

## MAIN TEXT

# Accurate simulation of cuff electrode stimulation predicting in-vivo strength-duration thresholds

Nathaniel Lazorchak  | M. Ryne Horn  | M. Ivette Muzquiz  |  
Landan M. Mintch | Ken Yoshida 

Department of Biomedical Engineering,  
Indiana University Purdue University  
Indianapolis, Indianapolis, Indiana,  
USA

## Correspondence

Ken Yoshida, PhD, Department of  
Biomedical Engineering, Indiana  
University Purdue University  
Indianapolis, 723 West Michigan Street,  
SL 220F, Indianapolis, IN 46202, USA.  
Email: [yoshidak@iupui.edu](mailto:yoshidak@iupui.edu)

## Funding information

National Institute of Biomedical  
Imaging and Bioengineering, Grant/  
Award Number: R21EB028469

## Abstract

**Background:** In-silico experiments used to optimize and inform how peripheral nerve based electrode designs perform hold the promise of greatly reducing the guesswork with new designs as well as the number of animals used to identify and prove promising designs. Given adequate realism, in-silico experiments offer the promise of identifying putative mechanisms that further inform exploration of novel stimulation and recording techniques and their interactions with bioelectric phenomena. However, despite using validated nerve fiber models, when applied to the more complex case of an implanted extracellular electrode, the in-silico experiments often do not compare quantitatively with the results of experiments conducted in in-vivo experiments. This suggests that the accuracy/realism of the environment and the lamination of the nerve bundle plays an important role in this discrepancy. This paper describes the sensitivity of in-silico models to the electrical parameter estimates and volume conductor type used.

**Methods:** In-vivo work was performed on rat vagus nerves ( $N = 2$ ) to characterize the strength-duration curve for various peaks identified in a compound nerve action potential (CAP) measured via a needle electrode. The vagus nerve has several distinct populations of nerve fiber calibers and types. Recruitment of a fiber caliber/type generates distinct peaks that can be identified, and whose conduction delay correlates to a conduction velocity. Peaks were identified by their recruitment thresholds and associated to their conduction velocities by the conduction delays of their peaks. An in-silico analog of the in-vivo experiment was constructed and experiments were run at the two extreme volume conductor cases: (1) The nerve in-saline, and (2) the nerve in-air. The specifically targeted electrical parameters were extraneural environment (in-air versus saline submersion), the resistivity ( $\rho$ ) of the epineurium and perineurium, and the relative permittivity ( $\epsilon_r$ ) of those same tissues. A time varying finite element method (FEM) model of the potential distribution vs time was quantified and projected onto a modified McIntyre, Richardson, and Grill (MRG), myelinated spinal nerve, active fiber model in NEURON to identify the threshold of activation as a function of

This is an open access article under the terms of the [Creative Commons Attribution-NonCommercial](https://creativecommons.org/licenses/by-nc/4.0/) License, which permits use, distribution and reproduction in any medium, provided the original work is properly cited and is not used for commercial purposes.

© 2022 The Authors. *Artificial Organs* published by International Center for Artificial Organ and Transplantation (ICAOT) and Wiley Periodicals LLC.



stimulus pulse amplitude versus pulse width versus fiber diameter. The in-silico results were then compared to the in-vivo results.

**Results:** The finite element method simulations spanned two macro environments: in-saline and in-air. For these environments, the resistivities for low and high frequencies as well as two different permittivity cases were used. Between these 8 cases unique cases it was found that the most accurate combination of those variables was the in-air environment for low-frequency resistivity ( $\rho_0$ ) and ex-vivo a measured permittivity ( $\epsilon_{r,\text{measured}}$ ) from unpublished ex-vivo experiments in canine vagal nerve, achieving a high degree of convergence ( $r^2 = 0.96$ ). As the in-vivo work was conducted in in-air, the in-air boundary condition test case was convergent with the in-silico results.

**Conclusions:** The results of this investigation suggest that increasing realism in simulations begets more accurate predictions. Of particular importance are ( $\rho$ ) and extraneural environment, with reactive electrical parameters becoming important for input waveforms with energy in higher frequencies.

#### KEYWORDS

finite element analysis, neural simulations, NEURON, threshold prediction

## 1 | INTRODUCTION

Since before the publication of the Hodgkin-Huxley model in 1952, researchers and scientists have sought to accurately predict and characterize neural activation thresholds.<sup>1</sup> Accurate prediction/realism not only has implications in basic scientific research but also plays a role in the development of new bioelectric methods to manipulate and interact with bioelectric phenomena, as techniques used in science translate towards application in therapies such as functional electrical stimulation (FES), bioelectric medicines, and neuromodulation.<sup>2,3</sup> Although accurate models involving channel dynamics or transmembrane behavior of space clamped membranes or neurons have been developed, the accuracy of predictions diminish when applied to implanted extracellular electrodes or surface electrodes, for example the TIME<sup>4</sup> and LIFE<sup>5</sup> intrafascicular electrodes and the FINE<sup>6</sup> and MCC<sup>7</sup> extrafascicular electrodes. Implanted or surface electrodes interact with the channels and the transmembrane potential in a very different manner than the space clamp modeled and used to validate the channel models. The space clamped transmembrane preparation is typically a patch of membrane or an attached neural soma, while the intracellular or surface electrode directly interacts with the transmembrane potential or current to characterize the state mechanics of the voltage sensitive channel.

Preparations used to test neural prosthetic electrodes involve the intact peripheral nerve bundle and fibers, along with the environmental tissues and electrode structure. The transmembrane potential evolves as a result

of the current density distributions and potentials that evolve through the volume conductor, as it interacts with the distributed capacitances and resistances of the nerve bundle and nerve fiber cables. Thus, the realism of the volume conductor, which includes the nerve bundle, the gaps between the electrode and nerve, and the surrounding environment, play an important role in the ultimate transmembrane potential and the activation/inactivation dynamics of the various voltage sensitive channels embedded in the neural membrane. Thus, there is a greater number of components and degree of complexity with the *in-silico* models of extracellular electrodes.

While in-silico models can inform design or make predictions, there remains large quantitative differences between model-based predictions and in-vivo measurements suggesting either a lack of realism or errors in the parameters used in the models. Although qualitative predictions matched in-vivo measurements, the absolute predicted values of thresholds or recordings are often orders of magnitude off. In order to assess whether the in-silico framework<sup>7-10</sup> or parameters used within the model were incorrect, a set of in-silico experiments were conducted where the electrode geometry and environment were identically captured from a set of in-vivo experiments. New characterizations of the nerve tissue and laminae conductivities and relative permittivities were made (unpublished results), and a new set of time dependent finite element simulations were imposed on a validated MRG nerve fiber model<sup>11</sup> that had been extended and translated to Python. The results of these combinations were then verified against the in-vivo strength-duration (SD)



curve experiment that the simulations were designed to replicate.

## 2 | METHODS

### 2.1 | In-vivo experiment

In-vivo experiments were conducted on a set of ( $N = 2$ ) female Sprague–Dawley rats. All experiments were conducted under a protocol approved by the IUPUI School of Science Institutional Animal Care and Use Committee (IUPUI SoS IACUC). A complete description of the animal preparation can be found in Ref. [12]. Briefly, anesthesia was induced using isoflurane (Vedco Inc., St. Joseph, MO, USA) using an intraperitoneal (IP) injection of urethane (800 mg/kg, Sigma-Aldrich Co., St. Louis, MO, USA) / alpha-chloralose (80 mg/kg, Arcos Organics, Fair Lawn, NJ, USA). It was maintained at the surgical plane using supplemental IP injections of the urethane/alpha chloralose compound. Surgical access to the left carotid artery and cervical vagus nerve was obtained through a midline incision of the skin overlying the trachea, followed by

blunt dissection to expose the cervical vagus nerve. A bipolar cuff electrode (CorTec GmbH, Freiburg, Germany) was placed around the cervical vagus nerve and used as the stimulating electrode. Rectangular pulses were delivered with pulse widths of 20, 60, 100, 110, 150, and 1000  $\mu$ s and pulse amplitude up to 0.3 mA to elicit all 5 peaks. This was delivered using an opto-isolated stimulator (DS3, Digitimer Ltd., Hertfordshire, UK) triggered by a pulse generator (33120A, Hewlett Packard, Engelwood, CO, USA). A recording unipolar needle electrode was placed caudal to the cuff electrode in the cervical vagus nerve, roughly 2.2 mm away from the cuffs closest contact and referenced to an indifferent needle electrode superficially embedded in one of the tracheal rings, as shown in Figure 1. Measurements were made with the nerve suspended in-air by the thickness of the cuff, with care taken to prevent drying of the nerve.

The cuff electrode used (Figure 1) had an inner diameter (ID) of 0.5 mm, contact width (CEW) of 0.5 mm, contact pitch (CEP) of 1.0 mm, and a contact-edge distance (CED) of 1.5 mm, and was used to deliver pulses of varying widths and amplitudes. Monophasic pulses were delivered to the cuff electrode, systematically varying the pulse

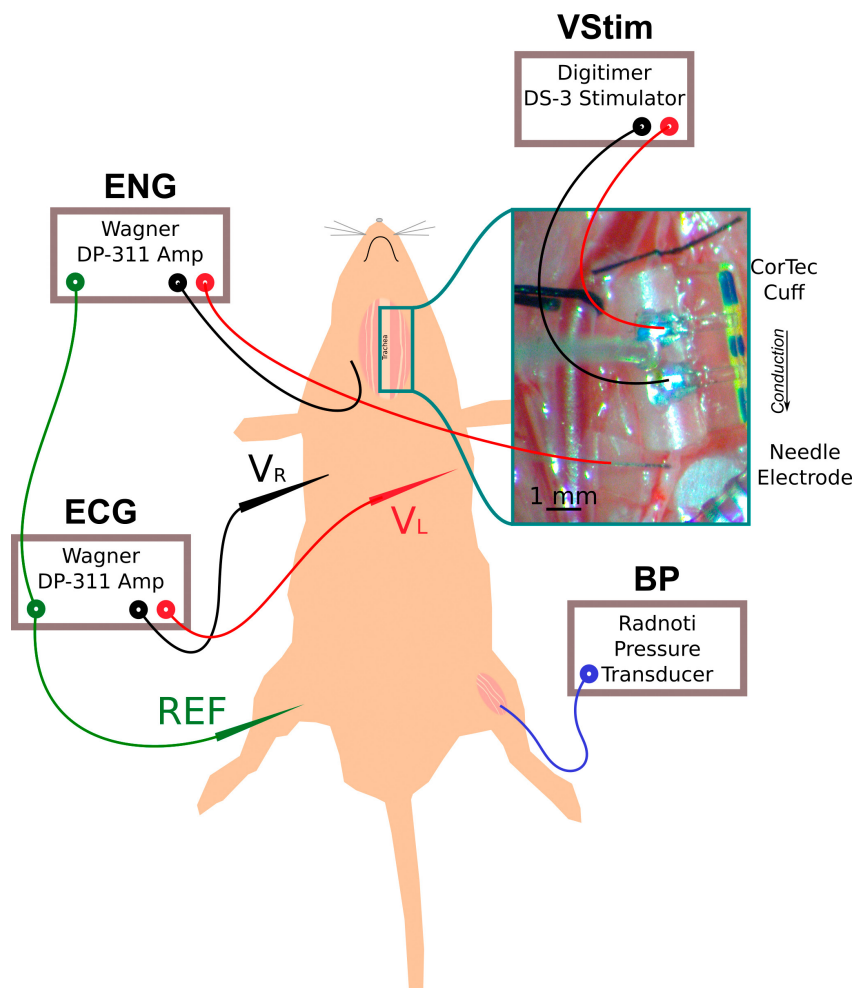


**FIGURE 1** In-vivo experimental configuration showing electrode placement on the rat vagus nerve and instrumentation used for pulse activation and recording the CAP along with changes to the rat's heart rate and blood pressure. The inset shows the proximal ligature, the CorTec bipolar cuff electrode used to initiate the CAP and recording needle electrode on the rat's left cervical vagus nerve. Adapted from Ref. [12]. [Color figure can be viewed at [wileyonlinelibrary.com](http://wileyonlinelibrary.com)]



width and pulse amplitude to capture the thresholds of the various nerve compound action potential (CAP) peaks detected by the needle electrode. A typical set of electro-neurogram (ENG) recordings are shown in Figure 2. The loci of thresholds for the first two peaks of the SD curves were quantified for comparison with the results of the in-silico experiments. The in-vivo experiments kept the nerve and electrodes moistened, but in-air and separated from surrounding tissues.

## 2.2 | Finite element model

An axial-symmetric model of a monofascicular nerve bundle, shown in Figure 3, was created within a finite

element method (FEM) modeling framework, COMSOL Multiphysics (V5.5, COMSOL Inc, Burlington, MA). The 0.4 mm diameter bundle is comprised of 3 discrete tissue layers: the 50  $\mu\text{m}$  thick epineurium, the 13  $\mu\text{m}$  thick perineurium, which is treated as a boundary with a surface thickness, and the endoneurium with a radius of 150  $\mu\text{m}$ . Around the middle of the nerve, a cuff electrode of equal geometric parameters to the bipolar cuff electrode was defined, and a 50  $\mu\text{m}$  gap was placed between cuff and nerve to simulate an imperfect fit. A saline environment was modeled as a domain that fills said gap and space around the cuff and nerve, plus an infinite element domain on the outside of the saline environment. Neumann boundary conditions were imposed on the outside of the infinite element domain through insulating boundaries and Dirichlet

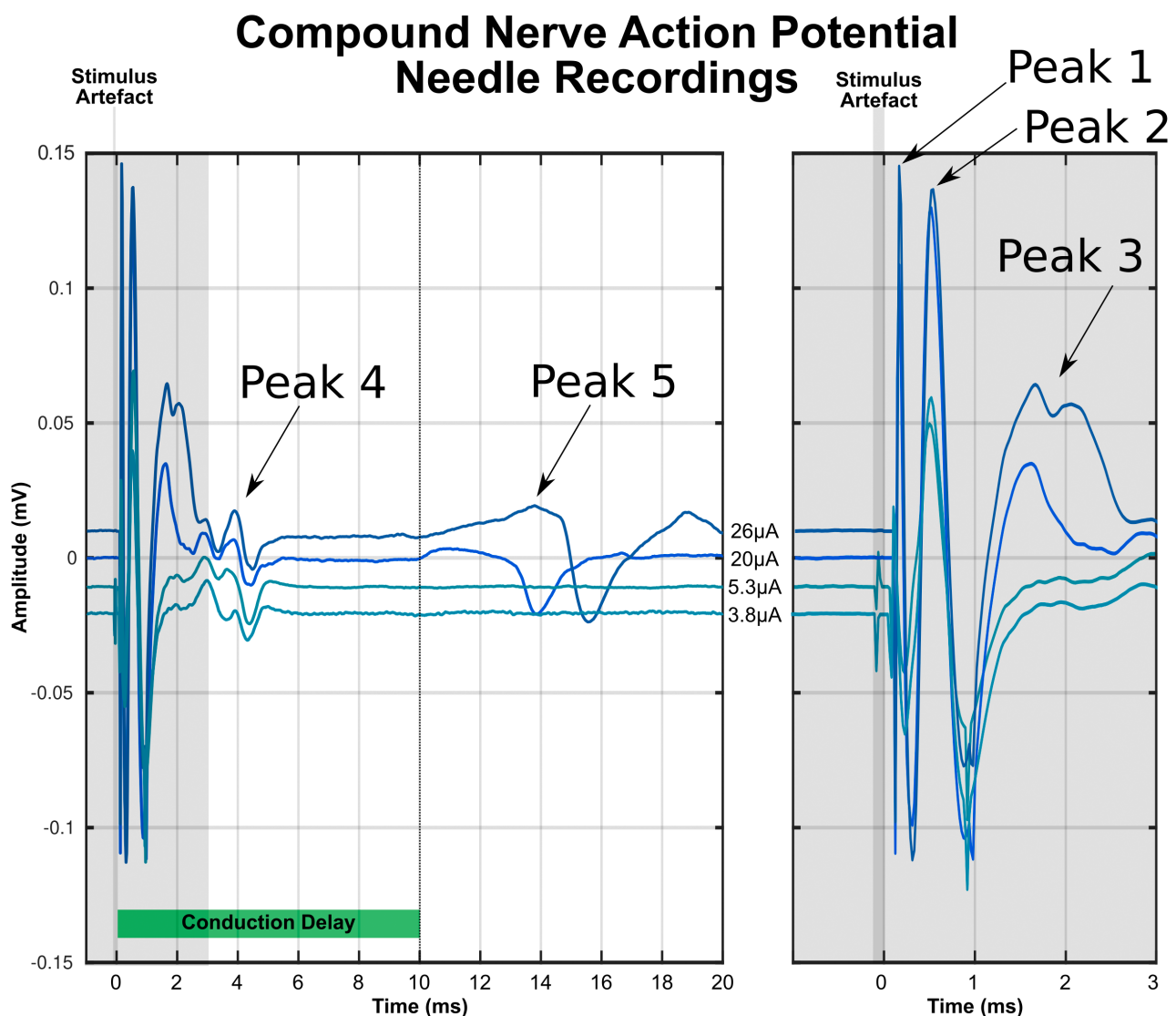
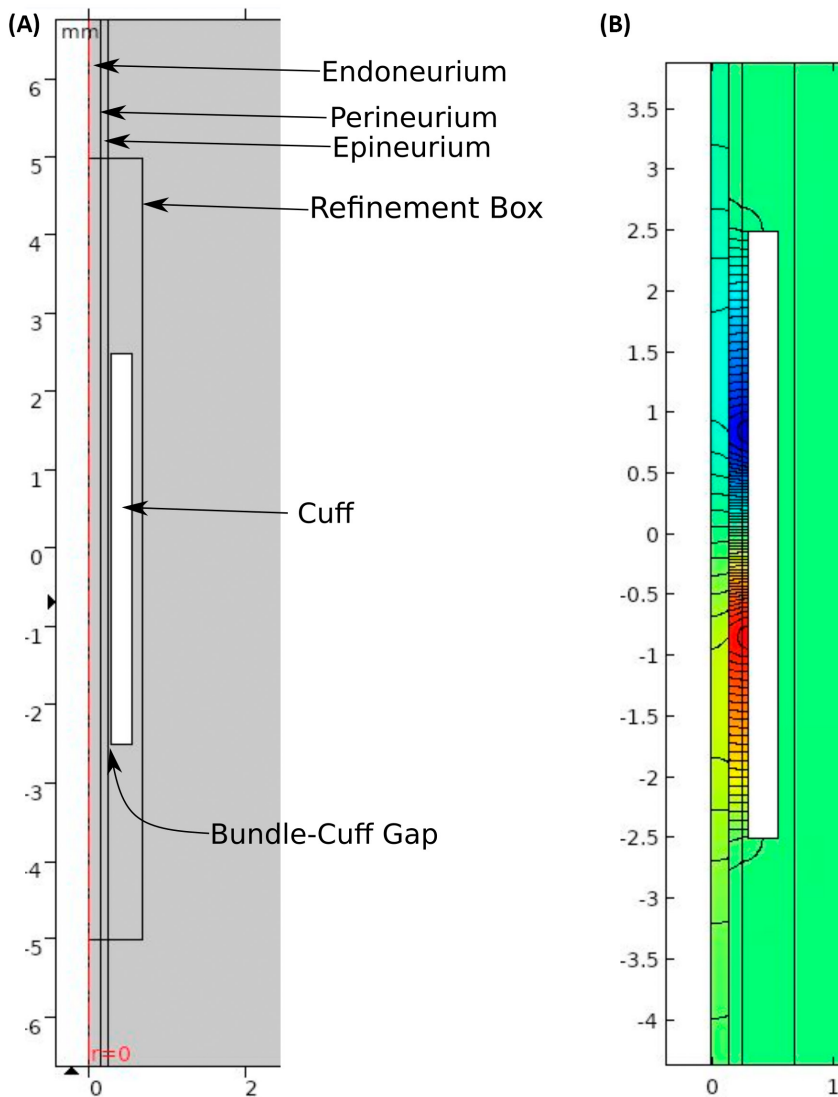


**FIGURE 2** Example of CAP recordings. Shown using conduction delay to the 5th peak for ease of visualization. This study used the thresholds of peaks 1 & 2 which correlate to myelinated A-fibers with calibers of  $\sim 11.5$  and  $\sim 6$   $\mu\text{m}$  were analyzed. Artifacts have been removed by shape subtraction and the waveforms are vertically shifted for viewing purposes, with dark gray showing the remaining stimulus artifact and lighter gray indicating the section shown to the right. [Color figure can be viewed at [wileyonlinelibrary.com](http://wileyonlinelibrary.com)]



**FIGURE 3** (A) Shows the in-silico geometry of the cuff about the nerve in a two-dimensional axial symmetric model. (B) Shows the steady state results of the simulation and the iso-potential lines. [Color figure can be viewed at [wileyonlinelibrary.com](http://wileyonlinelibrary.com)]



boundary conditions were imposed at the far distal ends of the model as grounds.

Simulated bipolar electrical stimulation was delivered through the cuff electrode contacts. The stimuli were a set of 1 A amplitude pulses of pulse widths between 30 and 1000  $\mu$ s with a 20  $\mu$ s rise/fall time. These simulations yielded the temporal and spatial evolution of the potential/current density distribution in the volume conductor of the model. Although inappropriate for use in animal experiments, and any value of current could have been defined for the model, 1 A was used in these simulations to simplify interpretation of the potential distribution created by the injection of current into the volume conductor, as the value of the coupling function becomes equal to the value of the potential directly about the nerve, or the extracellular potential ( $V_e$ ). The environment and the electrical parameters of the epineurium and perineurium serve as variables to evaluate which parameters gave the most realistic results. Two environments were evaluated, in-air and in-saline, as well as two versions each of resistivity,

$\rho$ , and relative permittivity,  $\epsilon_r$ . For resistivity, there were the low-frequency resistivity ( $\rho_0$ ) and high-frequency resistivity ( $\rho_\infty$ ). For relative permittivity,  $\epsilon_r$  the saline equivalent ( $\epsilon_{r,80}$ ) and ex-vivo measured values for perineurium ( $\epsilon_{r,\text{measured}}$ ) were used. See Table 1 for the values used.

The test cases changed epineurium and perineurium electrical resistivity and permittivity as follows: (A) in-saline  $\rho_0$  and  $\epsilon_{r,80}$ , (B) in-saline  $\rho_0$  and  $\epsilon_{r,\text{measured}}$ , (C) in-saline  $\rho_\infty$  and  $\epsilon_{r,80}$ , (D) in-saline  $\rho_\infty$  and  $\epsilon_{r,\text{measured}}$ , (E) in-air  $\rho_0$  and  $\epsilon_{r,80}$ , (F) in-air  $\rho_0$  and  $\epsilon_{r,\text{measured}}$ , (G) in-air  $\rho_\infty$  and  $\epsilon_{r,80}$ , and (H) in-air  $\rho_\infty$  and  $\epsilon_{r,\text{measured}}$ . Modeling an in-air environment was done through boundary conditions rather than the creation of a component with the electrical properties of air, as the resistivity of air is orders of magnitude greater than the modeled materials. The saline component was restricted to the gap between the electrode and the nerve, and all lateral boundaries were defined as insulators. The Dirichlet boundary conditions remained in place as grounds at the distal ends. Use of the in-air environment was implemented partially due to





Material	Conductivity (S/m)	Resistivity $\rho$ ( $\Omega \cdot m$ )	Relative permittivity $\epsilon_r$
Saline	1	1	80
Epineurium	$\sigma_0 = 0.015$	$\rho_0 = 68$	$\epsilon_{r,80} = 80$
	$\sigma_\infty = 0.79$	$\rho_\infty = 1.3$	$\epsilon_{r,measured} = 3.7e6$
Perineurium	$\sigma_0 = 0.00029$	$\rho_0 = 3460$	$\epsilon_{r,80} = 80$
	$\sigma_\infty = 0.037$	$\rho_\infty = 273$	$\epsilon_{r,measured} = 1440$
Endoneurium	{0.08, 0.08, 0.6} (diagonal tensor)	{12, 12, 1.7} (diagonal tensor)	80

TABLE 1 Electrical properties used in the finite element method model

Note: Epineurium and perineurium are from unpublished results from our lab and the endoneurium values from Ranck et al.<sup>13</sup>

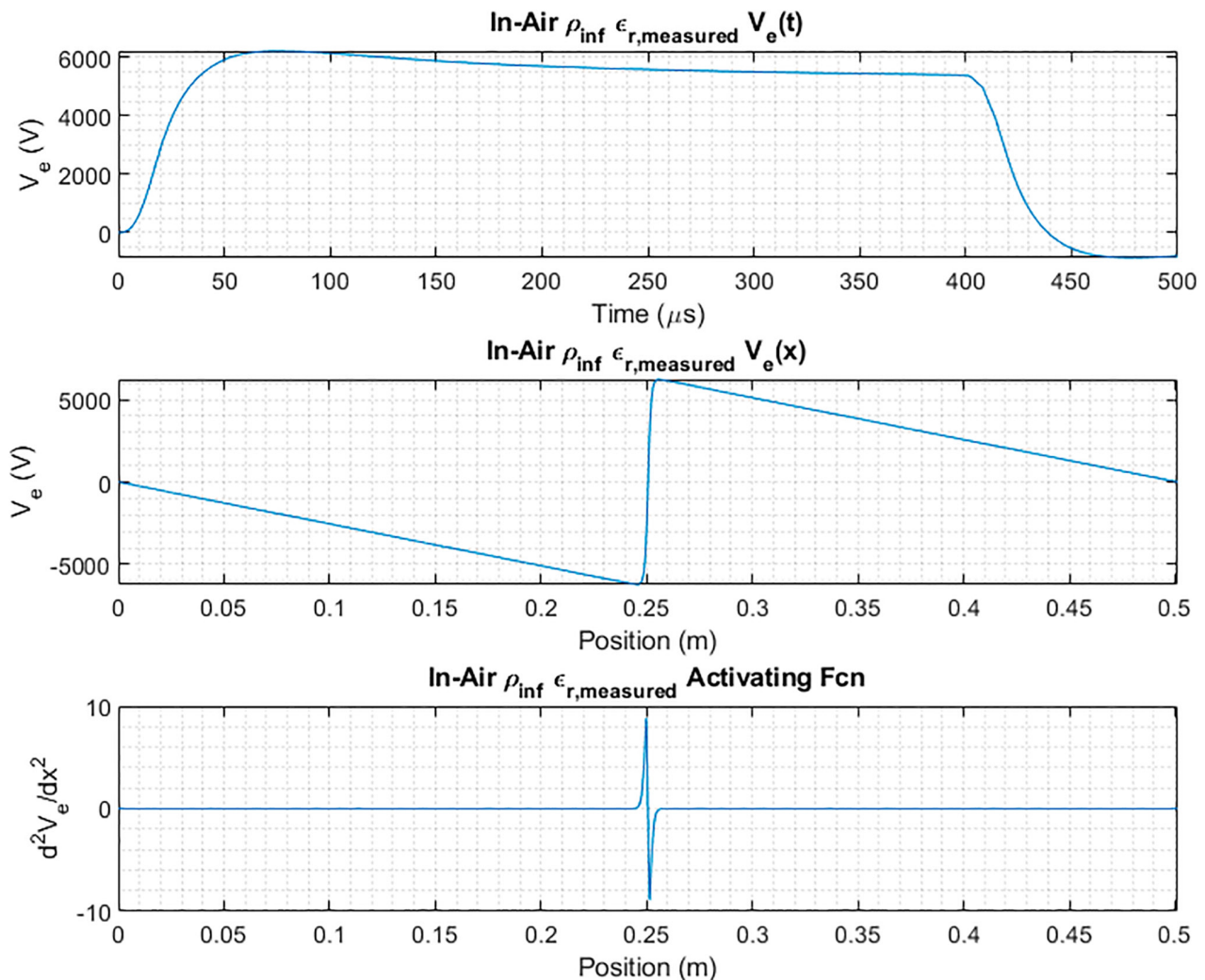


FIGURE 4 In-air, low frequency resistivity ( $\rho_0$ ), measured relative permittivity ( $\epsilon_{r,measured}$ ) 400  $\mu s$  pulse width weight and activating functions. [Color figure can be viewed at [wileyonlinelibrary.com](http://wileyonlinelibrary.com)]

the findings of Wu et al.'s study of the recording of neural action potential in lifted and non-lifted environments.<sup>14</sup>

The extracted value of the coupling function along the path of putative nerve axons, the weight functions, are derived from this model by taking the voltage developed across a line parallel to the axis within the endoneurium,

1  $\mu m$  inset from the perineurium. See Figure 4 for an example of a weight function  $V_e(x)$ , specifically the in-air  $\rho_0$  and  $\epsilon_{r,measured}$  weight extracted from the FEM model, as well as its activating function, which is proportional to the 2nd spatial derivative of  $V_e(t)$ ,<sup>15</sup> and the waveform applied at the fiber  $V_e(t)$ . Here, the activating function is

taken simply as the 2nd spatial derivative of  $V_e(t)$ . These weight functions are considered generalized with respect to axon/fiber diameter (FiberD), and differentiation between diameters occurs during later conditioning for the neural simulations.

For the purposes of comparison, the saline environment weights and activating functions are shown as Figure 5A, and the in-air environments as Figure 5B. It should be noted that, compared to the saline weights, the relative magnitude of the artificial electrodes is severely diminished in the in-air weights.

### 2.3 | NEURON nerve fiber model simulation

The active nerve fiber simulations were performed within the NEURON<sup>16</sup> (V7.7, Yale University) simulation environment using a version of the 2014 updated MRG<sup>11</sup>

model of peripheral nervous system (PNS) myelinated motor neuron axons. The modification to the MRG model was the conversion to Python (V3.7, Python Software Foundation, Wilmington DE) to enable programmatic definition of fiber diameter and the extension of the length of the fiber to 503 nodes of Ranvier to be able to accommodate the size of the weight functions extracted from the FEM model.

In order to incorporate the weight functions into a NEURON simulation, the weight functions were first conditioned into a NEURON compliant form within Matlab. For every desired fiber diameter, the weight function is first centered on the fiber, at a node of Ranvier (NoR), and interpolated in space such that there is a point for every defined segment of the model. The weight function and additional information are then sent to a Python script that initializes the model, defines the weight function as the  $V_e$ , and extracts desired data including the transmembrane current, transmembrane potential, and the gating variable values of the various embedded voltage sensitive channels. It also determines a time step based on the input to preserve stability and efficiency. Input modulation is done via direct scaling, assuming linearity within the FEM system.

Acquisition of in-silico SD curves was achieved through a Matlab script that runs simulations while performing a binary search through an array of values corresponding to peak  $V_e$  until it has two adjacent values with different activation states, of which the higher is considered the threshold value within the resolution of the test array, typically 1 mV. The script will continue this for every chosen weight function until the curve has been acquired.

In order to facilitate obtaining more detailed data and perform manual verification experiments, a Python script that saves transmembrane potential ( $V_m$ ),  $V_e$ , currents, and gating variables was used. MRG allows testing of fiber diameters between 5.7 and 16  $\mu\text{m}$ , with 11.5  $\mu\text{m}$  being the primary test case for these simulations.

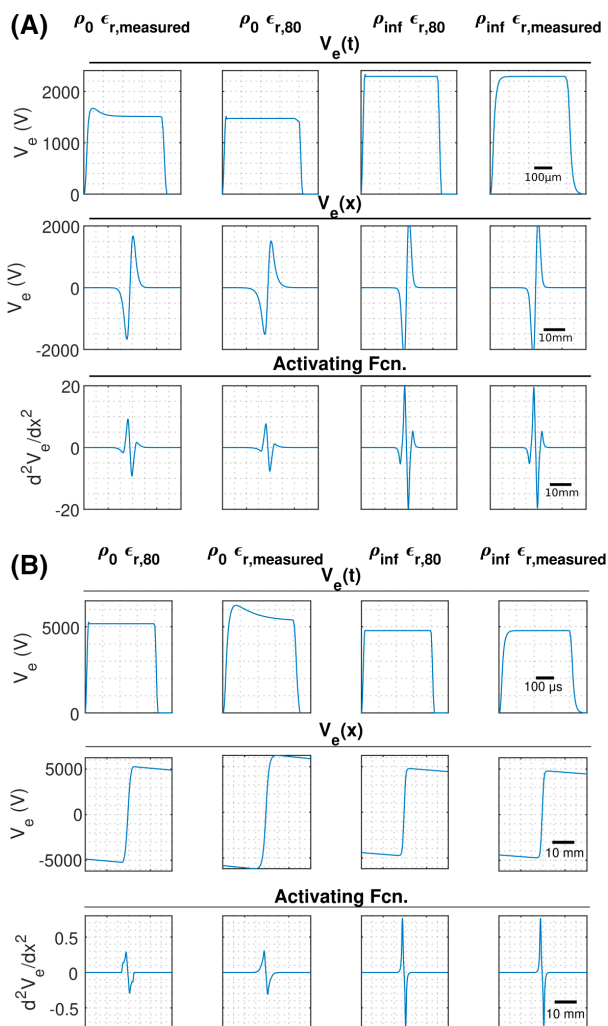
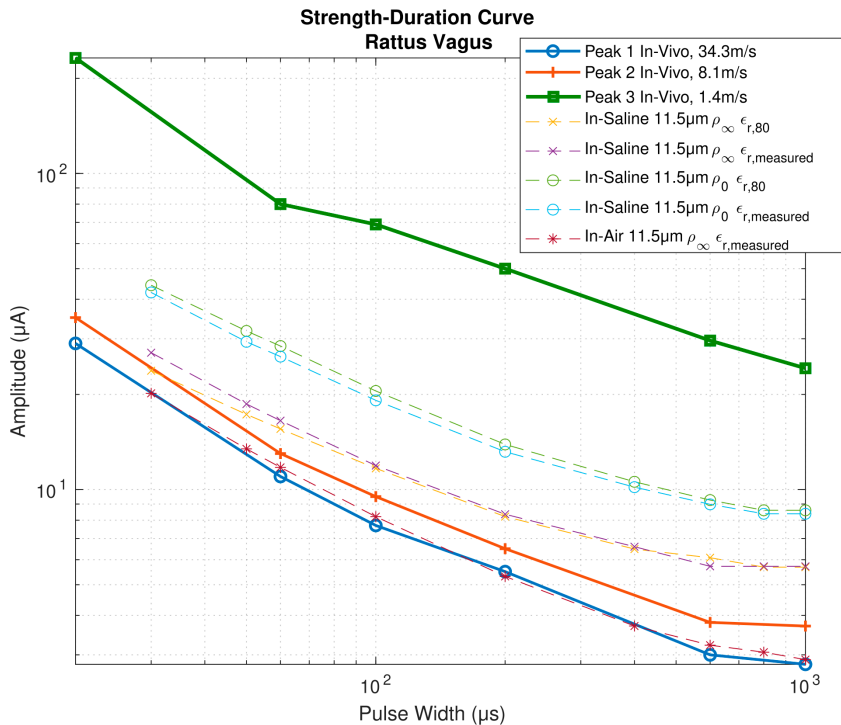


FIGURE 5 In-saline environment (A) and in-air environment (B) 400  $\mu\text{s}$  pulse width weight and activating functions. [Color figure can be viewed at [wileyonlinelibrary.com](http://wileyonlinelibrary.com)]

## 3 | RESULTS

### 3.1 | Electrical parameters and environment effects on thresholds

Environment and  $\rho$  had the greatest effect on thresholds, with  $\epsilon_r$  having less effect in these use cases. The best fit was found with the in-air  $\epsilon_{r,measured}$  weight on a 11.5  $\mu\text{m}$  fiber (conduction velocity of  $\sim 64$  m/s), corresponding to peak 1 in-vivo (conduction velocity  $\sim 23$  m/s), with a fit of  $r^2 = 0.96$ . Compared with the saline environment  $\rho_0, \epsilon_{r,80}$  weight at the same fiber diameter with  $r^2 = -0.13$ . The current thresholds can be seen in Figure 6.



**FIGURE 6** A log–log plot of the in-vivo thresholds for peaks 1–3 and in-silico strength-duration curves using the 11.5  $\mu\text{m}$  fiber diameter MRG model for different parameters. The peaks of the in-vivo measurements were estimated to have conduction velocities as follows: Peak 1 (34.3 m/s), Peak 2 (8.1 m/s), and Peak 3 (1.4 m/s). The fiber diameter estimated for Peak 1 is  $\sim 9.5 \mu\text{m}$ . However, peaks 2 and 3 are outside the conduction velocity range of simulated MRG fibers. There is clear separation between the saline based simulations and the in-air based simulation. Although all curves are within a factor of 10 to those measured in-vivo the best fit is with the in-air case for the SD curves for peaks 1 and 2. [Color figure can be viewed at [wileyonlinelibrary.com](http://wileyonlinelibrary.com)]

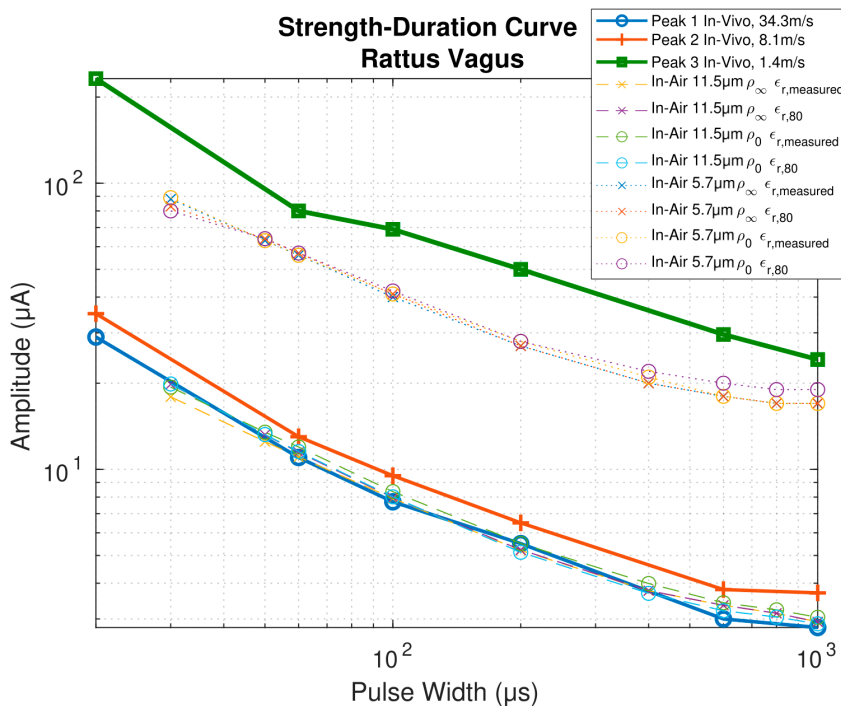


**FIGURE 7** A log–log plot of the in-vivo and in-silico in-air environment only SD curves using the 11.5 and 5.7  $\mu\text{m}$  fiber diameter MRG model. [Color figure can be viewed at [wileyonlinelibrary.com](http://wileyonlinelibrary.com)]

In contrast to the spread-out in-saline environment results, the in-air environment results are near to one another, as can be seen in Figure 7.  $r^2$  values for the in-air results range from approximately 0.87 to 0.96.

Notable in Figure 7 is a break from the trend seen in the saline environment results—the low frequency resistance results from bookends for the in-silico dataset, rather than being grouped as in Figure 6, showing an

increased sensitivity to relative permittivity as compared to the in-saline environment  $\rho_0$  cases. The  $\rho_\infty$  cases are comparatively unaffected.

Impedance is the origin of a substantial portion of the variation in the current thresholds. Impedance is the coupling variable between voltage and current, thus despite smaller changes in  $V_e$ , the stimulus current changed substantially due to the in-air simulation requiring less



current to produce an equivalent  $V_e$ . As seen in Figure 8, the in-air weights show a significantly higher effective impedance, owing to the removal of the diminutive parallel resistance offered by the saline environment. Two effects of  $\epsilon_r$  can be seen in Figure 8; In the  $\epsilon_{r,measured}$  weights,  $V_e$  is attenuated at low pulse widths due to the increase in capacitance and thus time constant of the intermediate tissues increasing leading to a cessation of input before achieving steady state. In the  $\rho_0$  cases, there is also a sizable difference in the steady-state impedance as  $\epsilon_r$  varies. The in-air results show an approximately 16% reduction in impedance while the saline environment results show an approximately 9% reduction in impedance.

### 4 | DISCUSSION

The results indicate a large degree of convergence between the in-vivo and in-silico results which brings the two within a factor of 10 of one another. The difference can be explained by the tightness of the electrode to the nerve bundle and the geometrical variations that might exist between the perfect cylinders used in the model versus those conditions that exist in the actual in-vivo case. Additionally, these results match closely with in-vivo results from Pelot and Grill's results for 2 to 25 m/s strength duration curve.<sup>17</sup> Additionally, this work brings the realism between in-vivo and in-silico into even closer

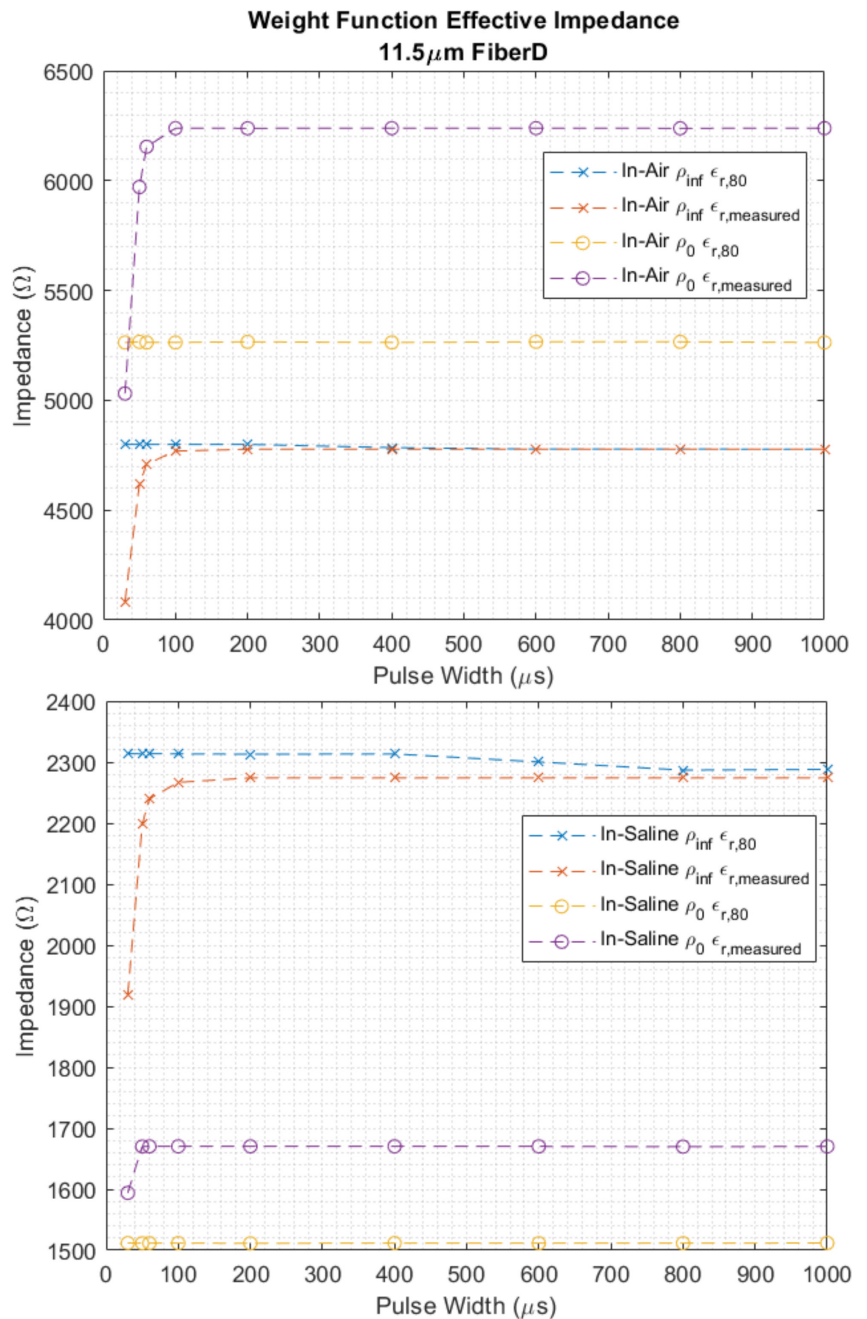


FIGURE 8  $|Z|$  as a function of pulse width for in-saline environment (top) and in-air environment (bottom) weight functions. [Color figure can be viewed at [wileyonlinelibrary.com](http://wileyonlinelibrary.com)]



agreement than previous work by Rattay et al.,<sup>18</sup> by bringing the strength-duration curve for their in-vivo results down by nearly an order of magnitude and in close agreement with our in-vivo results. The in-air 11.5  $\mu\text{m}$  fiber simulations are in agreement with Peak 1, which corresponds to a fiber with a conduction velocity of 34 m/s and a diameter of  $\sim 7 \mu\text{m}$ , according to the conduction velocity curve from in-silico results. The in-silico conduction velocity results, gained through tracking difference in time between a single traveling action potential passing two points a known distance apart, yielded a slope of 6.3 m/s per micrometer fiber diameter ( $\frac{m}{s \cdot D}$ ), higher than both McIntyre et al.<sup>11</sup> at  $4.6 \frac{m}{s \cdot D}$  for small diameters and  $5.66 \frac{m}{s \cdot D}$  for large diameters, and the classical work of Hursh<sup>19</sup> at  $6.0 \frac{m}{s \cdot D}$ . Peak 2 with an estimated 8.1 m/s conduction velocity have thresholds that are slightly higher than those for Peak 1. Its slower conduction velocity suggests a smaller fiber diameter, but its conduction velocity lies outside of the range of simulated MRG fibers. Nonetheless, a higher threshold is expected for fibers with smaller diameters. The fiber type for Peak 3 is also unclear but is likely either an A $\delta$  or C fiber. The MRG spinal nerve fiber was selected for these in-silico experiments since the fiber was validated in Ref. [11] along with its strength duration curve. Unlike the simulations in their paper, where the strength duration curve was obtained by simulating the transmembrane activation characteristics of the nerve fiber and compared against in-vivo fibers, the present work compares nerve fibers activated using a bipolar nerve cuff electrode in-vivo versus the exact same case in-silico.

#### 4.1 | Potential issues and sources of error

Some factors should be understood in relation to these simulations. The MRG model is of A $\alpha$  nerve fibers in the somatic spinal peripheral nerve. As such, the defined nerve fiber calibers are much larger than those comprising autonomic peripheral nerves such as the vagus nerve. Moreover, the MRG models comprise a set of motor neuron axons based on human, cat, and rat experiments, and validated against rat motor neuron data. In the present work, the in-vivo experiment was performed on the vagus nerve of a rat. Extrapolation from somatic motor neurons to autonomic nerve fibers was needed and could constitute a source of error. However, the two major factors dictating activation and propagation of the action potential are the cable properties of the nerve fiber, and the activation dynamics of the fast voltage gated sodium channel, Na<sub>v</sub>1.7. The former dictates the length in which a depolarization on the nerve fiber carries to move the depolarization wavefront, and thus the conduction velocity. The

former dictates the thresholds of activation needed to initiate the action potential. Should, for example, membrane time constants differ, then the chronaxies will differ and accuracy will be lost at low pulse widths.

Another possible source of error lies in geometry and the comparison of single fiber action potential (SFAP) thresholds to CAP thresholds. The in-silico model is a perfectly symmetrical, monofascicular nerve while in reality, the vagus nerve is asymmetrical and multifascicular. To compare SD curves, two primary assumptions must be made: First, despite the geometric disparities between model and reality, the developed  $V_e$  is consistent. Second, that the CAP becomes measurable at the same point as the single fiber in the position equivalent to that modeled activates. The errors listed have been either been mitigated (e.g., the simulation dt) or otherwise considered negligible.

#### 4.2 | Effects of electrical parameters and environment on activation

In terms of raw thresholds, the environment and the resistivity play the largest parts, as they most directly impact the magnitude of the extracellular potential developed by a single current. The effects of  $\epsilon_r$  are primarily seen at low pulse widths, as higher widths allow  $V_e$  to reach and maintain a steady state (see Figure 8), diminishing the ability of  $\epsilon_r$  to effect the threshold, though not eliminating it as seen most clearly in the in-air results (Figure 7).

Where  $\epsilon_r$  is most likely to have a large effect is with input waveforms with frequencies in higher ranges, such as in simulations of kHz block, as time constant increases proportionally to  $\epsilon_r$ , decreasing corner frequency and thus increasing high frequency attenuation.

Like threshold, activation function morphology is also affected primarily by environment and  $\rho$  through the ability of simulated current to nearly circumnavigate the cuff and create virtual electrodes. Figure 5 shows that having a lower  $\rho$  increases the relative magnitude of the virtual electrodes, while Figure 4 shows that the in-air simulated environment eliminates the virtual electrodes, as current has no alternate path to ground with the exception of the far end of the nerve.

Generally speaking, the electrical parameters have slightly different effects in the in-air cases. For example, in Figure 5B, for the  $\rho_0$  case, using  $\epsilon_{r,80}$  creates a sharp decline in the activation function due to current, once outside of the cuff, being forced through a medium whose resistivity far overpowers its permittivity, leading to a sudden shift to a linear trend in potential outside of the cuff. The other cases either have a stronger permittivity or weaker resistivity allowing for smoothing of the activation and weight



functions or a secondary conductive medium, i.e., saline, allowing current to escape and diffuse.

### 4.3 | Uncertainty in the model fit

As is always the case, a model is only as accurate as the assumptions made. Although the SD curves had a difference in magnitudes well within a factor of 10, there are still issues with aligning conduction velocities seen in-vivo and calculated in-silico, recall that the 11.5  $\mu\text{m}$  simulated in-air fiber aligned well with the first peak of the in-vivo results, the simulated conduction velocity was around  $\sim 64$  m/s whereas the calculated in-vivo conduction velocity for peak 1 was around  $\sim 23$  m/s. These assumptions include fiber length, temperature differences, and the location of activation are areas where error can arise. Preliminary observations in our lab have shown that bulk strains at  $<3\%$  of the fiber length have been seen to cause internal displacements of the bands of Fontana. This leads to the possibility that the internal structural reorganization caused by an applied displacement may impact the conduction velocity. For the in-vivo experiments the rat was kept warm by a warm water jacket under the animal as well as a heat lamp from the top side. Within the incision at the neck the vagus suspended in the air to insulate it from other sources of noise, however this incision area was exposed to the ambient area and was likely cooled a few degrees from body temperature, this would in-turn slow the conduction velocity down of the CAP peaks. Another large factor is the area in which the nerve activates. In the in-vivo experiments the stimulation threshold was minimized by looking at swapping the polarity of the stimulation. As such, it is reasonable to assume that cathodic activation occurred on the contact closest to recording electrode, however, the exact location of this activation will vary with the stimulus amplitude. A way to get around this would have been to place two recording electrodes and measure the conduction velocity by observing the delay between the two recordings. The physical geometry of the in-vivo incision area limited our ability to fit another recording electrode in the preparation. As a result of a single recording point, the onset of the CAP peaks would be the onset of an action potential which is where the time point used in calculating the conduction velocity should be sampled, however this can be exceedingly difficult in the presence of low signal-to-noise ratio. Additionally, CAP peaks 3–5 could very well be the result of EMG crosstalk as this prep was not entirely mechanically isolated from the body, even in-air this signal can find its way to the recording electrode.

In the in-vivo prep the nerve was in-air to improve the signal-to-noise ratio of the compound action potentials being recorded by the needle electrode. A byproduct of this was the imposed removal of the leakage currents outside of the nerve bundle volume, leading to a best-case scenario in terms of lowering the SD curve. Conversely, the in-saline case simulated in-silico would realistically maximize the leakage currents that could be expected in an in-vivo prep where the incision area is flooded with saline, or the case of a chronically implanted electrode. Simulating these two cases was meant to give estimates of the lower and upper threshold of expected results. These bounds are however tied up with the many assumptions listed above and as such are subject to variability.

## 5 | CONCLUSION

These results suggest that realism in simulation paradigm begets more accurate predictions. The model used was able to achieve reasonable convergence, provided the acceptance of mapping one species to another. Of particular importance to SD curves are  $\rho$  and the extraneural environment, and the results suggests that  $\epsilon_r$  becomes more important for input waveforms with energy predominantly in higher frequencies, roughly 10 kHz or greater.

### AUTHOR CONTRIBUTIONS

Nathaniel Lazorchak performed NEURON simulations, wrote analysis scripts, analyzed, and interpreted results, and drafted the article. M. Ryne Horn performed COMSOL simulations, wrote conversion scripts, and helped interpret results. M. Ivette Muzquiz led the in-vivo experiment, wrote analysis script to deal with in-vivo results, and analyzed and interpreted in-vivo results. Landan M. Mintch performed the in-vivo surgery. Ken Yoshida directed the overall work, trained the students on surgical placement and running of the experiment, and wrote custom Matlab analysis scripts. All authors reviewed and edited the manuscript.

### ACKNOWLEDGEMENT

The authors also acknowledge the support of the Department of Biomedical Engineering Research Assistantship program for funding Mr. Horn, Ms. Muzquiz, and Mr. Mintch. The authors thank Dr. John Schild for the maintenance of the animal protocol and for training Mr. Mintch on surgical procedures. The authors acknowledge major research support for the work from a NIH R21 Trailblazer grant (R21EB028469).

### CONFLICT OF INTEREST

The authors have no conflict of interest.




## DATA AVAILABILITY STATEMENT

The data that support the findings of this study are available and can be obtained following a reasonable request to the corresponding author.

## ETHICS STATEMENT

All experiments were carried out under a protocol approved by the IUPUI School of Science Institutional Animal Care and Use Committee (IUPUI SoS IACUC). They were performed in accordance with the Guide for the Care and Use of Laboratory Animals (National Institutes of Health Publication. No. 85-23, Revised 2011).

## ORCID

Nathaniel Lazorchak  <https://orcid.org/0000-0002-7631-1695>

M. Ryne Horn  <https://orcid.org/0000-0002-1066-6303>

M. Ivette Muzquiz  <https://orcid.org/0000-0002-8657-6101>

Ken Yoshida  <https://orcid.org/0000-0003-4566-580X>

## REFERENCES

1. Irnich W. The terms “chronaxie” and “rheobase” are 100 years old. *Pacing Clin Electrophysiol.* 2010 Apr;33(4):491–6.
2. Watanabe T, Futami R, Hoshimiya N, Handa Y. An approach to a muscle model with a stimulus frequency-force relationship for FES applications. *IEEE Trans Rehab Eng.* 1999 Mar;7(1):12–8.
3. Parker JL, Shariati NH, Karantonis DM. Electrically evoked compound action potential recording in peripheral nerves. *Bioelectron Med.* 2018 Jan;1(1):71–83.
4. Boretius T, Badia J, Pascual-Font A, Schuettler M, Navarro X, Yoshida K, et al. A transverse intrafascicular multichannel electrode (TIME) to interface with the peripheral nerve. *Biosens Bioelectron.* 2010 Sep 15;26(1):62–9.
5. Malagodi MS, Horch KW, Schoenberg AA. An intrafascicular electrode for recording of action potentials in peripheral nerves. *Ann Biomed Eng.* 1989 Jul;17(4):397–410.
6. Tyler DJ, Durand DM. Functionally selective peripheral nerve stimulation with a flat interface nerve electrode. *IEEE Trans Neural Syst Rehabil Eng.* 2002 Dec;10(4):294–303.
7. Choi AQ, Cavanaugh JK, Durand DM. Selectivity of multiple-contact nerve cuff electrodes: a simulation analysis. *IEEE Trans Biomed Eng.* 2001 Feb;48(2):165–72.
8. Chemineau ET, Schnabel V, Yoshida K. A modeling study of the recording selectivity of longitudinal intrafascicular electrodes. In: Getting FES into clinical practice, proceedings of IFESS-FESet 2004, 9th Annual Conference of the international functional electrical stimulation society and the 2nd conference of FESnet, 6–9 September 2004. Bournemouth, UK. p. 378–80.
9. Qiao S, Yoshida K. Influence of unit distance and conduction velocity on the spectra of extracellular action potentials recorded with intrafascicular electrodes. *Med Eng Phys.* 2013 Jan;35(1):116–24.
10. Horn MR, Holinsky B, Struijk JJ, Alfrey KA, Schild JH, Yoshida K. In-silico biophysical myelinated and unmyelinated autonomic nerve fiber models. In: Program Book, 22nd Annual Conference of the International Functional Electrical Society. Nottwil, Switzerland; 2018. p. 115–8.
11. McIntyre CC, Richardson AG, Grill WM. Modeling the excitability of mammalian nerve fibers: influence of afterpotentials on the recovery cycle. *J Neurophysiol.* 2002 Feb 1;87(2):995–1006.
12. Muzquiz MI, Mintch L, Horn MR, Alhawwash A, Bashirullah R, Carr M, et al. A reversible low frequency alternating current nerve conduction block applied to mammalian autonomic nerves. *Sensors.* 2021 Jul 1;21(13):4521.
13. Ranck JB Jr, BeMent SL. The specific impedance of the dorsal columns of cat: an anisotropic medium. *Exp Neurol.* 1965 Apr;11(4):451–63.
14. Wu G, Belzberg A, Nance J, Gutierrez-Hernandez S, Ritzl EK, Ringkamp M. Solutions to the technical challenges embedded in the current methods for intraoperative peripheral nerve action potential recordings. *J Neurosurg.* 2019 Aug;133(3):884–93.
15. Rattay F. Analysis of models for external stimulation of axons. *IEEE Trans Biomed Eng.* 1986 Oct;33(10):974–7.
16. Carnevale T, Hines M. *The NEURON book.* Cambridge: Cambridge University Press; 2006. p. 457.
17. Pelot NA, Grill WM. In vivo quantification of excitation and kilohertz frequency block of the rat vagus nerve. *J Neural Eng.* 2020 Mar 9;17(2):026005.
18. Rattay F, Paredes LP, Leao RN. Strength-duration relationship for intra- versus extracellular stimulation with microelectrodes. *Neuroscience.* 2012 Jul 12;214:1–13.
19. Hursh JB. Conduction velocity and diameter of nerve fibers. *Am J Physiol Legacy Content.* 1939 Jul 31;127(1):131–9.

**How to cite this article:** Lazorchak N, Horn MR, Muzquiz MI, Mintch LM, Yoshida K. Accurate simulation of cuff electrode stimulation predicting in-vivo strength-duration thresholds. *Artif Organs.* 2022;46:2073–2084. <https://doi.org/10.1111/aor.14374>